

An *in vivo* pig model for testing novel PET radioligands targeting cerebral protein aggregates

1 Nakul Ravi Raval ^{1,2}, Arafat Nasser ¹, Clara Aabye Madsen ^{1,2}, Natalie Beschorner ³, Emily
2 Eufaula Beaman ¹, Morten Juhl ⁴, Szabolcs Lehel ⁵, Mikael Palner ^{1,6,7}, Claus Svarer ¹, Pontus
3 Plavén-Sigray ¹, Louise Møller Jørgensen ^{1,2,8}, Gitte Moos Knudsen ^{*1,2}

4 ¹ Neurobiology Research Unit, Copenhagen University Hospital (Rigshospitalet), Copenhagen,
5 Denmark

6 ² Faculty of Health and Medical Sciences, University of Copenhagen, Copenhagen, Denmark

7 ³ Center for Translational Neuromedicine, University of Copenhagen, Copenhagen, Denmark

8 ⁴ Cardiology Stem Cell Centre, Copenhagen University Hospital (Rigshospitalet), Copenhagen,
9 Denmark

10 ⁵ Department of Clinical Physiology, Nuclear Medicine & PET, Copenhagen University Hospital
11 (Rigshospitalet), Copenhagen, Denmark

12 ⁶ Department of Clinical Research, Clinical Physiology and Nuclear Medicine, University of
13 Southern Denmark, Odense, Denmark

14 ⁷ Department of Nuclear Medicine, Odense University Hospital, Odense, Denmark

15 ⁸ Copenhagen Spine Research Unit, Copenhagen University Hospital (Rigshospitalet), Glostrup,
16 Denmark

17
18 *** Correspondence:**
19 Gitte Moos Knudsen
20 Neurobiology Research Unit
21 Section 8057, Rigshospitalet
22 Blegdamsvej 9
23 DK-2100 Copenhagen Ø
24 Denmark
25 Email: gmk@nru.dk

26 **Keywords:** Positron emission tomography, [¹¹C]PIB, protein injection model, alpha-synuclein,
27 amyloid-beta, brain imaging, autoradiography, large animal PET

28

29 Abstract

30 Positron emission tomography (PET) has become an essential clinical tool for diagnosing
31 neurodegenerative diseases with abnormal accumulation of proteins like amyloid- β or tau. Despite
32 many attempts, it has not been possible to develop an appropriate radioligand for imaging aggregated
33 α -synuclein in the brain for diagnosing, e.g., Parkinson's Disease. Access to a large animal model
34 with α -synuclein pathology would critically enable a more translationally appropriate evaluation of
35 novel radioligands.

36 We here establish a pig model with cerebral injections of α -synuclein preformed fibrils or brain
37 homogenate from postmortem human brain tissue from individuals with Alzheimer's disease (AD) or
38 dementia with Lewy body (DLB) into the pig's brain, using minimally invasive surgery and validated
39 against saline injections. In the absence of a suitable α -synuclein radioligand, we validated the model
40 with the unselective amyloid- β tracer [^{11}C]PIB, which has a high affinity for β -sheet structures in
41 aggregates. Gadolinium-enhanced MRI confirmed that the blood-brain barrier was intact. A few
42 hours post-injection, pigs were PET scanned with [^{11}C]PIB. Quantification was done with Logan
43 invasive graphical analysis and simplified reference tissue model 2 using the occipital cortex as a
44 reference region. After the scan, we retrieved the brains to confirm successful injection using
45 autoradiography and immunohistochemistry.

46 We found four times higher [^{11}C]PIB uptake in AD-homogenate-injected regions and two times
47 higher uptake in regions injected with α -synuclein-preformed-fibrils compared to saline. The
48 [^{11}C]PIB uptake was the same in non-injected (occipital cortex, cerebellum) and injected (DLB-
49 homogenate, saline) regions. With its large brains and ability to undergo repeated PET scans as well
50 as neurosurgical procedures, the pig provides a robust, cost-effective, and good translational model
51 for assessment of novel radioligands including, but not limited to, proteinopathies.

52 1. Introduction

53 Several neurodegenerative diseases share the pathology of misfolded proteins (Lázaro et al., 2019),
54 and positron emission tomography (PET) neuroimaging has become the primary imaging modality to
55 precisely diagnose and quantify such proteinopathies in patients. As of now, many suitable PET
56 radioligands are in use for neuroimaging of amyloid- β and tau (Mathis et al., 2017); these aggregated
57 proteins are seen in diseases such as Alzheimer's disease (AD), frontotemporal dementia, and
58 progressive supranuclear palsy. By contrast, attempts to develop a suitable radioligand for
59 neuroimaging of α -synuclein aggregates or inclusions, the hallmark of Parkinson's disease (PD),
60 multiple system atrophy, and dementia with Lewy bodies (DLB) have largely failed. A PET
61 radioligand targeting α -synuclein would critically assist in an earlier and more precise diagnosis,
62 which would be helpful for both the patient and clinician and it could facilitate development of
63 efficacious treatments.

64 In preclinical studies, some radioligands have shown promise for detection of α -synuclein aggregates
65 (Hooshyar Yousefi et al., 2019; Capotosti et al., 2020; Kaide et al., 2020; Kuebler et al., 2020), as
66 described in an extensive review on small molecules PET imaging of α -synuclein (Korat et al., 2021).
67 Nevertheless, because of lack of specificity or affinity to α -synuclein, no tracers have succeeded in
68 translating to humans. α -synuclein radioligands may also require higher selectivity and affinity due to
69 the lower aggregated protein pathology seen in α -synucleinopathies compared to the extensive
70 pathology seen in amyloid- β - and tauopathies (Braak and Braak, 2000; Lashuel et al., 2013).

71 Moreover, α -synuclein inclusions are mostly intracellularly located which may make them less
72 accessible to radioligands compared to extracellular amyloid- β aggregates.

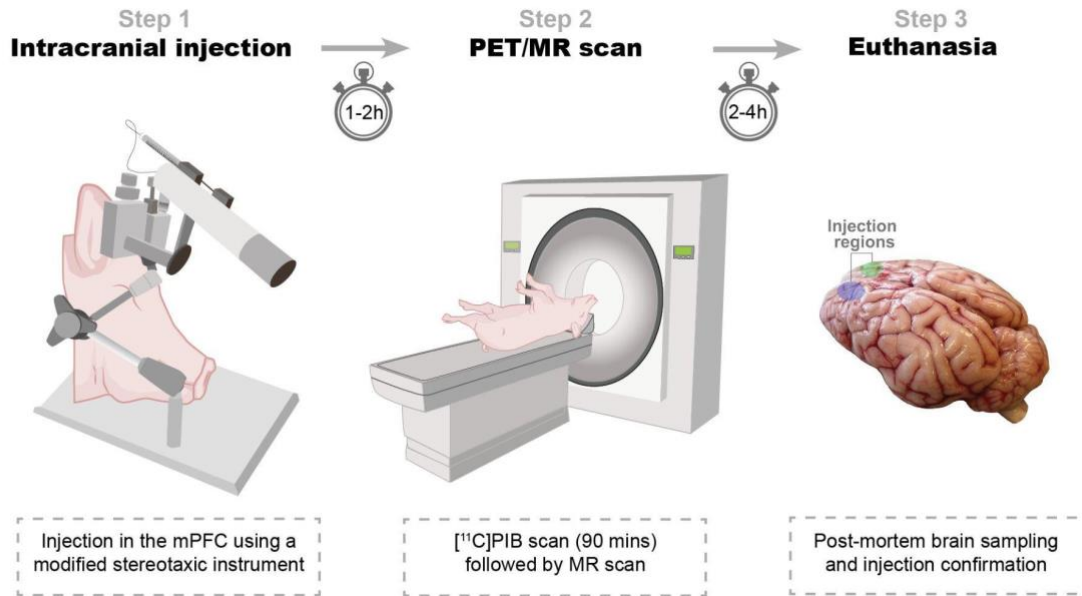
73 A particular challenge has been an unmet need for appropriate α -synuclein animal models. Novel
74 PET radioligands are often initially tested in rodents due to lower costs and availability of disease
75 models, then translated to higher species, including humans. Tracers with low rodent brain uptake are
76 often quickly discarded although it is known that rodents have higher efflux transporter activity than
77 larger animals (Shalgunov et al., 2020). Rodent proteinopathy models also do not entirely resemble
78 human pathology, making it difficult to predict novel radioligands' performance in higher species.
79 That is, access to an appropriate large animal proteinopathy model would substantially advance the
80 evaluation of novel radioligands for neuroimaging, e.g., α -synuclein and reduce the risk of failure due
81 to poor translation from *in vitro* to humans. The pig has become an attractive alternative to
82 nonhuman primates which are associated with high costs, feasibility, repeatability, and not the least,
83 the use is associated ethical concerns (Harding, 2017).

84 We here propose the use of domestic pigs with intracerebral protein injections as a suitable
85 translational model for testing new radioligands. We and others have previously made widespread
86 use of the pig for this purpose (Parker et al., 2012; Ettrup et al., 2013; Hansen et al., 2014;
87 Winterdahl et al., 2014; Donovan et al., 2020) because the pig has high predictive value for a
88 successful translation to humans. In our pig model here, we make intracerebral injections of either α -
89 synuclein preformed fibrils, postmortem AD human brain homogenate (containing amyloid- β and tau
90 pathology), postmortem DLB human brain homogenate with pure α -synuclein pathology, and control
91 these injections with saline. Due to the absence of an appropriate α -synuclein radioligand, we
92 validate our model using [^{11}C]PIB, a non-specific radioligand for amyloid- β (Klunk et al., 2004),
93 which also has affinity to α -synuclein preformed fibrils but not to Lewy bodies (Ye et al., 2008). To
94 confirm the integrity of the blood-brain barrier, we conducted gadolinium-enhanced MRI scan and to
95 confirm brain pathology, we characterized the injected brain regions with immunohistochemistry and
96 autoradiography.

97 2. Methods

98 2.1 Animals

99 Seven female domestic pigs (crossbreed of Landrace \times Yorkshire \times Duroc) weighing on average
100 27 ± 1 kg (ranging from 25-31 kg) and approximately 10-11 weeks old were used in the present study
101 (Table 1). Animals were sourced from a local farm and prior to any experiments. They were
102 acclimatized for 7-9 days in an enriched environment. All animal procedures were performed
103 following the European Commission's Directive 2010/63/EU, approved by the Danish Council of
104 Animal Ethics (Journal no. 2017-15-0201-01375), and complied with the ARRIVE guidelines. The
105 overall design of the study is shown in Figure 1.



106

107 **Figure 1.** Study design. *Step 1*: Intracerebral injections. α -synuclein preformed fibrils, Alzheimer's
108 disease human brain homogenate, dementia with Lewy bodies human brain homogenate, or saline is
109 injected in either hemisphere. *Step 2*: PET/MR scan. Animals are PET scanned with [¹¹C]PIB. Some
110 animals are also MRI scanned in a 3T scanner. *Step 3*: Euthanasia. After the final scan, animals are
111 euthanized, their brains removed, and injection sites' pathology confirmed.

112 **2.2 Preparation and surgical procedure**

113 Pigs were injected in the medial prefrontal cortex (mPFC) with 25 μ L of α -synuclein preformed
114 fibrils (6.4 mg/mL), AD human brain homogenate (10% homogenate in saline), DLB human brain
115 homogenate (10% homogenate in saline), or saline (Table 1). The details and characteristics of the
116 preformed fibrils and human brains are provided in the supplementary information (Supplementary
117 Table 1). The substrates were injected in both hemispheres, as detailed for each pig in Table 1, and in
118 accordance with our procedure for targeting mPFC (Jørgensen et al., 2017, 2018).

119 A detailed description of preparation, anesthesia and transport has previously been described by us
120 (Jørgensen et al., 2021). Briefly, anesthesia was induced by intramuscular (IM) injection of Zoletil
121 mixture and maintained with 10-15 mg/kg/h intravenous (IV) propofol infusion. Analgesia was
122 achieved with 5 μ g/kg/h fentanyl IV infusion. Endotracheal intubation allowed for ventilation with
123 34% oxygen in normal air at 10-12 mL/kg. The left and right femoral arteries were catheterized with
124 Seldinger Arterial Catheter (Arrow International, Inc., Reading, PA, USA). The left and right
125 superficial mammary veins and ear veins were also catheterized. A urinary catheter was placed to
126 avoid discomfort and stress throughout the surgery and scanning schedule. The animals were
127 monitored for heart rate, blood pressure, peripheral oxygen saturation (SpO₂), end-tidal CO₂
128 (EtCO₂), blood glucose, and temperature throughout the scan, except while undergoing MRI scans.

129 Intracerebral injections were performed using a modified stereotaxic approach: An in-house
130 instrument for modified stereotaxic procedures containing a head-rest plate, a flexible arm attached
131 with a micro-manipulator (World Precision Instruments, Sarasota, FL, USA), and a micro-syringe
132 infusion pump system (World Precision Instruments, Sarasota, FL, USA) (Supplementary Figure 1).
133 The flexible arm allowed the micro-manipulator to be positioned and fixed relative to the target entry

134 point with a trajectory perpendicular to the skull, as illustrated in Supplementary Figure 1. For the
135 first two experiments (Pig 1 and 2), we used a prototype of the device with slightly less arm
136 flexibility and a different micro-manipulator brand and syringe-type, although the capacity, needle
137 size, length, and tip shape were the same. However, the prototype did provide injections comparable
138 to the remaining ones, as validated with immunohistochemistry.

139 After installation of local anesthesia, midline incision, and skull exposure, two burr holes were
140 placed bilaterally, 25 mm anterior and 8 mm lateral to bregma, followed by hemostasis and dura
141 puncture. We have previously validated this target point: 8, 25, 14 mm in the X, Y, Z coordinate
142 relative to bregma, to center on grey matter in the mPFC (Jørgensen et al., 2017, 2018). The syringe
143 and the needle were then positioned and fixed in a trajectory perpendicular to the skull and with the
144 needle tip adjusted to the skull entry point. The syringes (250 μ L SGE Gas-tight Teflon Luer Lock
145 Syringes (World Precision Instruments, Sarasota, FL, USA) [different syringes for the different
146 injectates]) were attached with SilFlex tubing (World Precision Instruments, Sarasota, FL, USA),
147 NanoFil Injection Holder (World Precision Instruments, Sarasota, FL, USA) and 28 G Hamilton Kel-
148 F hub blunt tip needle (Hamilton Central Europe, Giarmata, Romania). The SilFlex tubing and
149 NanoFil Injection Holder were removed during homogenate injection because of the viscous content.

150 Using the micromanipulator, the needle was slowly advanced to the mPFC target point
151 (perpendicular to the skull). The injection was performed over two steps with 10 μ L, and 15 μ L
152 injected 1 mm apart (centered at the mPFC target point). The infusion was delivered at 450 nL/min
153 using the micro-syringe infusion pump followed by a 7-minute pause before a slow withdrawal of the
154 needle to avoid backflow. After the procedure, both burr holes were packed with an absorbable
155 hemostatic gelatin sponge (Curaspon[®], CuraMedical BV, Assendelft, Netherlands), and the incision
156 was sutured shut. The animals were then transported to the scanner facilities and connected to the
157 respirator.

158 **Table 1.** Overview of animals. Bodyweight, injection substance, injected dose/mass of [¹¹C]PIB, and
159 availability of parent fraction curve, and gadolinium contrast MR scan.

Pig no.	Weight (kg)	Injection in the left injection site	Injection in the right injection site	Injected dose [¹¹ C]PIB (MBq)	Injected mass [¹¹ C]PIB (μ g)	Individual parent fraction curve	Gd-MRI scan
1	28	α -syn-PFF	α -syn-PFF	500	1.72	✓	-
2	27	α -syn-PFF	Saline	492	1.85	✓	-
3	25	Saline	α -syn-PFF	378	2.43	✓	✓
4	28	α -syn-PFF	DLB-homogenate	440	7.94	✓	✓
5	31	DLB-homogenate	AD-homogenate	447	13.49	-	✓
6	28	DLB-homogenate	AD-homogenate	461	3.97	-	-
7	27	Saline	AD-homogenate	424	2.34	-	-

α -syn-PFF = α -synuclein preformed fibrils (160 μ g/25 μ L)

Saline = physiological saline (25 μ L)
DLB-homogenate = Dementia with Lewy bodies human brain homogenate (10%, 25 μ L) [Braak stage II, n = 2 x2 regions, A β and tau -ve]
AD-homogenate = Alzheimer's disease human brain homogenate (10%, 25 μ L) [Braak stage IV, n = 2 x2 regions, α -syn -ve]
Gd-MR scan = Gadolinium-enhanced MRI

160

161 **2.3 PET scanning protocol and radiochemistry**

162 All pigs were PET-scanned with a Siemens high-resolution research tomograph (HRRT) scanner
163 (CPS Innovations/Siemens, Malvern, PA, USA). [^{11}C]PIB was prepared at the Copenhagen
164 University Hospital, Rigshospitalet, as per routine clinical preparation. The complete method of
165 preparation is explained in the supplementary information (Supplementary Figure 2). Data
166 acquisition lasted 90 min after bolus injection (over ~20 s) of [^{11}C]PIB through one of the superficial
167 mammary veins (IV). The injected dose was 448 ± 41 MBq, while injected mass was 4.82 ± 4.3 μ g
168 (mean \pm SD).

169 **2.4 Blood sampling and HPLC analyses**

170 Manual arterial blood samples were drawn at 2.5, 5, 10, 20, 30, 40, 50, 70, and 90 min after injection,
171 while an ABSS autosampler (Allogg Technology, Strängnäs, Sweden) continuously measured arterial
172 whole blood radioactivity during the first 20 min. The manual blood samples were measured for total
173 radioactivity in whole blood and plasma using an automated gamma counter (Cobra 5003; Packard
174 Instruments, Downers Grove, CT, USA) cross-calibrated against the HRRT. Radiolabeled parent and
175 metabolite fractions were determined in plasma using an automatic column-switching radio-high
176 performance liquid chromatography (HPLC) as previously described (Gillings, 2009), equipped with
177 an extraction column Shim-pack MAYI-ODS (50 μ m, 30 x 4.6 mm; Shimadzu Corporation, Kyoto,
178 Japan) eluting with 50 mM HNa₂PO₄ pH 7.0 and 2% isopropanol (v/v) at a flow rate of 3 mL/min,
179 and an Onyx Monolithic C18 analytical column (50 x 4.6 mm, Phenomenex, Torrance, CA, USA)
180 eluting with 26% acetonitrile and 74% 100 mM HNa₂PO₄ pH 7.0 (v/v) at a flow rate of 3 mL/min.
181 Before analysis by radio-HPLC, the plasma samples were filtered through a syringe filter (Whatman
182 GD/X 13 mm, PVDF membrane, 0.45 μ m pore size; Frisenette ApS, Knebel, Denmark). Plasma was
183 diluted 1:1 with the extraction buffer, and up to 4 mL of plasma sample was used. The eluent from
184 the HPLC system was passed through the radiochemical detector (Posi-RAM Model 4; LabLogic,
185 Sheffield, UK) for online detection of radioactive parent and metabolites. Eluents from the HPLC
186 were collected with a fraction collector (Foxy Jr FC144; Teledyne, Thousand Oaks, CA, USA), and
187 fractions were counted offline in a gamma well counter (2480 Wizard2 Automatic Gamma Counter,
188 PerkinElmer, Turku, Finland). The parent fraction was determined as the percentage of the
189 radioactivity of the parent to the total radioactivity collected. Examples of radio-HPLC
190 chromatograms from a pig are shown in Supplementary Figure 3.

191 **2.5 Gadolinium-contrast MRI scanning protocol**

192 The integrity of the BBB post-intracerebral injection was assessed by determining the %-difference
193 ΔT_1 -map of the pre-gadolinium and the post-gadolinium scans. The MRI data were acquired on a 3T
194 Prisma scanner (Siemens, Erlangen, Germany) using a human 64-channel head coil (active coil
195 elements were HC3-7 and NC1). Three pigs were scanned in the MRI scanner as previously
196 described by us (Jørgensen et al., 2021). The pigs underwent two T1-map scans: pre-and post-
197 gadolinium contrast injection. The protocol for T1-weighted 3D magnetization-prepared rapid
198 gradient-echo (MP-RAGE) MRI was: frequency direction = anterior to posterior; dimension= 144 x
199 256 x 256; slice thickness = 0.9 mm; repetition time = 2000 ms; echo time = 2.58 ms; inversion time

200 = 972 ms; flip angle = 8°; base resolution = 256 x 256, and acquisition time = 192 s. After the pre-
201 gadolinium T1-map scan, pigs received gadolinium IV (0.1 mmol/kg, Gadovist® [gadobutrol], Bayer
202 A/S, Copenhagen, Denmark) through a superficial mammary vein and were rescanned 5 mins later
203 with another T1-map scan. Data were processed using a custom code in MATLAB 9.5.0 (R2018b)
204 (The MathWorks Inc., Natick, MA, USA). DICOM files were converted to NIfTI-1 using dcm2niix
205 (Li et al., 2016). The post-gadolinium T1-map was co-registered and resliced to the pre-gadolinium
206 T1-map using SPM12. A %-difference map (ΔT_1 -map) was created from the resliced post-
207 gadolinium and pre-gadolinium T1-maps (Equation 1). Three regions in the ΔT_1 -map were
208 measured: left injection site, right injection site, and occipital cortex

209
$$\Delta T_1 \text{ map} = \left(\frac{\text{Post_gadolinium } T_1 \text{ map} - \text{Pre_gadolinium } T_1 \text{ map}}{\text{Pre_gadolinium } T_1 \text{ map}} \right) \times 100 \text{ (Equation 1)}$$

210 **2.6 [³H]PIB autoradiography**

211 At the end of the scanning, the animals were euthanized by IV injection of 20 mL
212 pentobarbital/lidocaine. After euthanasia, the brains were removed, snap-frozen with powdered dry-
213 ice, and stored at -80°C until further use. 20 µm coronal cryosections were sectioned on a cryostat
214 (Thermo Scientific/Epredia™ CryoStar™ NX70 Cryostat, Shandon Diagnostics Limited, Runcorn,
215 UK) and mounted on Superfrost Plus™ adhesion microscope slides (Thermo Fisher Scientific,
216 Waltham, MS, USA). Sections were stored at -80°C for the remaining period of the study.

217 We performed [³H]PIB (Novandi Chemistry AB, Södertälje, Sweden, Molar activity: 78 Ci/mmol)
218 autoradiography to calculate the total available binding sites (B_{\max}) and equilibrium dissociation
219 constant (K_D) in the injected pig brain, and compared this to the B_{\max} and K_D of human brain regions
220 that were used to create the homogenates. We performed saturation assays using increasing
221 concentrations of [³H]PIB for total binding and [³H]PIB + thioflavin S (100 µM) for non-specific
222 binding on AD-homogenate-injected pig brain slices (n=1, 0 to 5 nM of [³H]PIB), α -synuclein-
223 preformed-fibril-injected pig brain slices (n=1, 0 to 5 nM of [³H]PIB), and AD post-mortem human
224 brain slices (n=2 x 2 regions, 0 to 40 nM of [³H]PIB). Since there was no specific binding in DLB-
225 homogenate-injected pig slices or DLB human brain slices, we could not perform saturation assays
226 on these sections. Human brain slices were prepared in the same fashion as pig brain slices, including
227 section thickness and storage. Detailed procedure for autoradiography is available in the
228 supplementary information.

229 The data were analyzed using GraphPad Prism (v. 9.2.0; GraphPad Software, San Diego, CA, USA).
230 Non-linear regression analysis (Function: One site - total and non-specific binding) was used to
231 calculate B_{\max} and K_D values for all three assays. The fitting method used was the least squared
232 regression with no weighting. In vitro binding potential (BP) was calculated with Equation 2.

233

234
$$BP = \frac{B_{\max}}{K_D} \text{ (Equation 2)}$$

235 **2.7 PET data reconstruction and preprocessing**

236 PET list-mode emission files were reconstructed using the OP-3D-OSEM algorithm, including
237 modeling the point-spread function, with 16 subsets, ten iterations, and standard corrections (Sureau
238 et al., 2008). During reconstruction, attenuation correction was performed using the MAP-TR μ -map
239 (Keller et al., 2013). Emission data were binned into time frames of increasing lengths: 6 x 10 s, 6 x

240 20 s, 4 × 30 s, 9 × 60 s, 2 × 180 s, 8 × 300 s, 3 × 600 s. Each time frame consisted of 207 planes of
241 256 × 256 voxels of 1.22 × 1.22 × 1.22 mm in size.

242 Brain parcellation was done with our previously published automatic PET-MR pig brain atlas method
243 (Villadsen et al., 2017). The neocortex, occipital cortex, and cerebellum non-vermis (henceforth
244 denoted as the cerebellum) were extracted from the Saikali atlas (Saikali et al., 2010) for the present
245 study. Two additional regions for the injection site were hand-drawn on the atlas from an
246 approximate injection site that was initially characterized around the site of needle penetration as
247 visualized by the MRI scans and postmortem extracted brain. This was also further confirmed and
248 optimized by positive immunohistochemistry slices from the region (Supplementary Figures 4 and
249 5). Regions approximately 0.32-0.35 cm³ (~ 250 voxels) in size were placed symmetrically in the left
250 and right hemispheres. This region is slightly larger than the injection site itself, but this gives leeway
251 for any potential mechanical error during the stereotactic operation. Wherever possible (not possible
252 in, e.g., saline-injected regions), the automatic region was visually inspected with late-scan frames
253 averaged.

254 Regional radioactivity concentration (kBq/mL) was normalized to injected dose (MBq) and corrected
255 for the animal weight (kg) to provide standardized uptake values (SUV, g/mL) used to make average
256 plots as in Figure 2. PMOD 3.7 (PMOD Technologies, Zürich, Switzerland) was used to visualize
257 and create the representative PET and MR images.

258 **2.8 Kinetic modeling**

259 Kinetic modeling was performed using *kinfitr* (v. 0.6.0) (Matheson, 2019; Tjerkaski et al., 2020) in R
260 (v. 4.0.2; "Taking Off Again," R core team, Vienna, Austria). The Logan Graphical Analysis was
261 applied to estimate the total volume of distribution (V_T) values (Logan et al., 1990), using a
262 metabolite corrected input function derived from radioactivity measurements of arterial blood
263 samples. Reference tissue modeling was performed with the simplified reference tissue model 2
264 (SRTM2), with an average k_{2'}, to calculate non-displaceable binding potential (BP_{ND}) using the
265 occipital cortex as the reference region (Yaqub et al., 2008). For more details on the kinetic
266 modeling, see supplementary information.

267 **2.9 Statistical analyses**

268 Graph-Pad Prism (v. 9.2.0; GraphPad Software, San Diego, CA, USA) was used for data
269 visualization and statistical analysis. All data are presented as mean values ± standard deviation. The
270 difference in PET outcomes (Logan V_T and SRTM2 BP_{ND}) between the injected regions and
271 reference tissues was calculated using the non-parametric Kruskal-Wallis one-way analysis of
272 variance (ANOVA). For assessment of change in gadolinium-contrast MR, we used the Friedman
273 non-parametric ANOVA test with paired testing. Post-hoc ANOVA tests were corrected for multiple
274 comparisons by Dunn's multiple comparison test (Dunn, 1964).

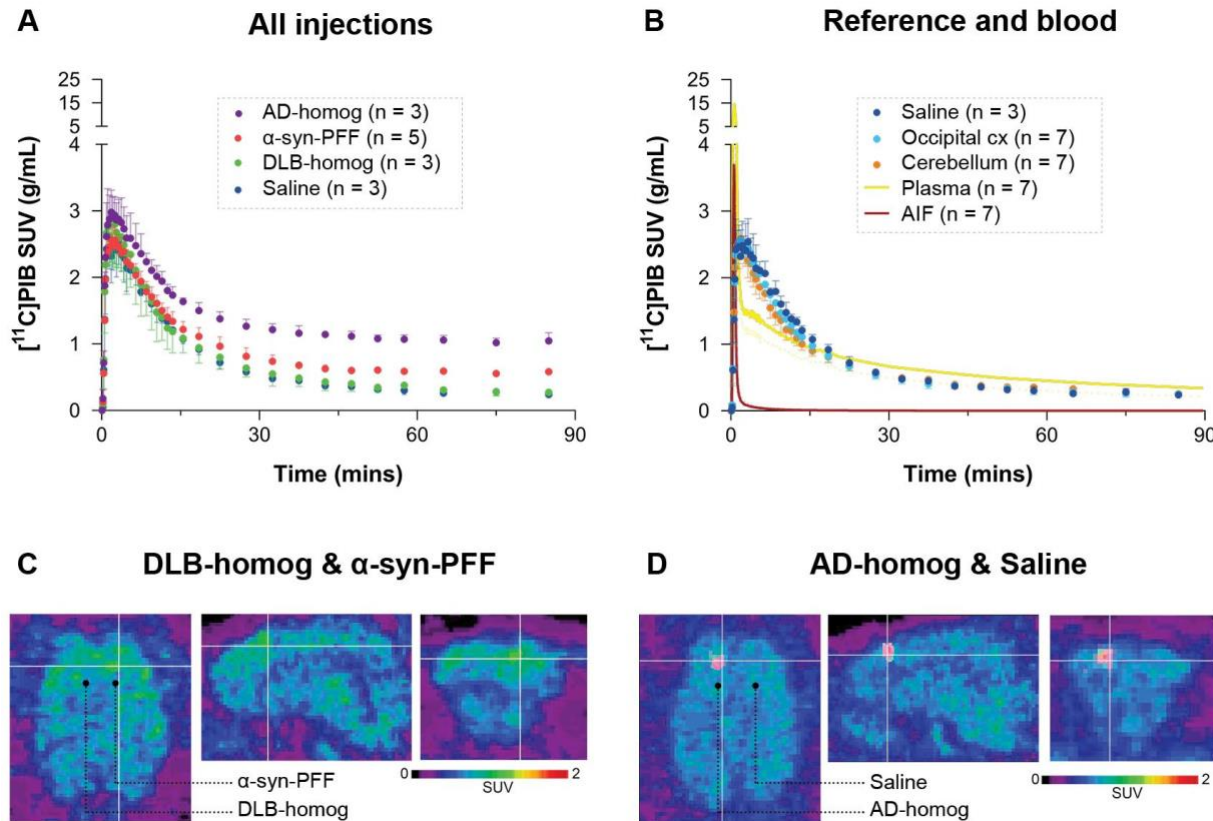
275 **3 Results**

276 **3.1 [¹¹C]PIB time-activity curves**

277 After [¹¹C]PIB injection, we observed high brain uptake and rapid tracer wash-out. The blood and
278 brain kinetics of [¹¹C]PIB were very fast, with less than 10% of the parent radioligand remaining in
279 plasma after 2.5 mins (Figure 2 and Supplementary Figure 6). We found higher radioactivity
280 retention in the AD-homogenate- and α-synuclein-preformed-fibrils injected region (Figure 2A).

281 Compared to the cerebellum and the occipital cortex, almost no retention was seen in DLB-
282 homogenate and saline-injected regions (Figure 2A and B).

283



284

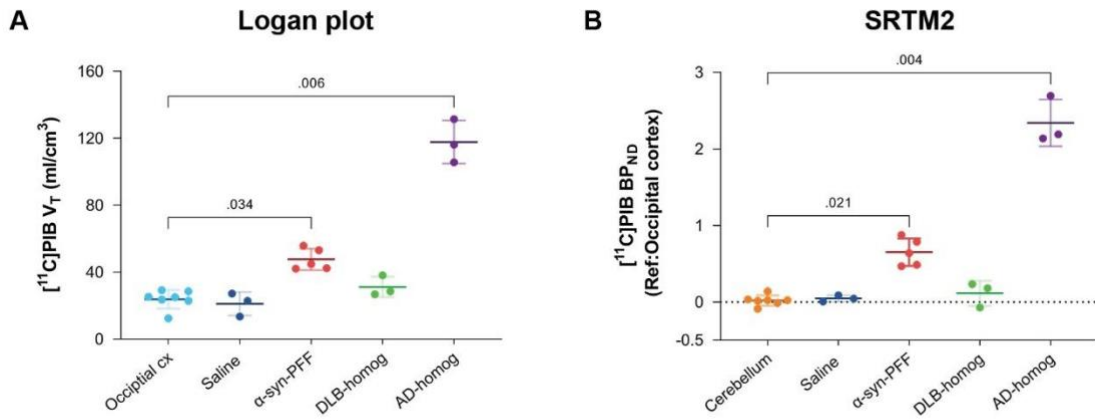
285 **Figure 2.** Regional time-activity curves of $[^{11}\text{C}]$ PIB in A) the different injection regions and B) the
286 reference regions and saline-injected region with the uncorrected plasma curve and arterial input
287 function. Representative summed PET across the entire duration of the scan (0-90 mins) images
288 showing injection regions including C) SUV scaled brain images including the brain areas injected
289 with α -synuclein preformed fibrils or DLB homogenate and D) AD homogenate or saline.

290 3.2 Kinetic modeling of $[^{11}\text{C}]$ PIB

291 $[^{11}\text{C}]$ PIB binding parameters from Logan graphical analysis and SRTM2 are summarized in Table 2.
292 We found 4-fold higher V_T values in the AD-homogenate injected region compared to the occipital
293 cortex ($p = 0.006$) and 2-fold higher V_T values in the α -synuclein-preformed fibrils region ($p = 0.034$)
294 (Figure 3A). We found no difference between the saline- and DLB-injected regions.

295 Compared to the cerebellum, the average BP_{ND} of 2.34 was higher ($p = 0.004$) in the AD-homogenate
296 injected region, and the average BP_{ND} of 0.65 was also higher ($p=0.016$) in the α -synuclein-
297 preformed-fibrils injected region. There was no difference in BP_{ND} in the saline- or DLB-homogenate
298 injected regions compared to the cerebellum (Figure 3B).

299



300

301 **Figure 3.** Kinetic modeling of $[^{11}\text{C}]PIB$. A) Kinetic modeling with arterial input (Logan). Direct
 302 comparison of V_T values in the different injection regions to the occipital cortex. B) Kinetic modeling
 303 with occipital cortex as a reference region (SRTM2). BP_{ND} values are compared to the cerebellum.

304 **Table 2.** Summary of kinetic modeling outcomes of $[^{11}\text{C}]PIB$. All values denote the mean \pm standard
 305 deviation. PFF=preformed fibrils. NA= not applicable.

306

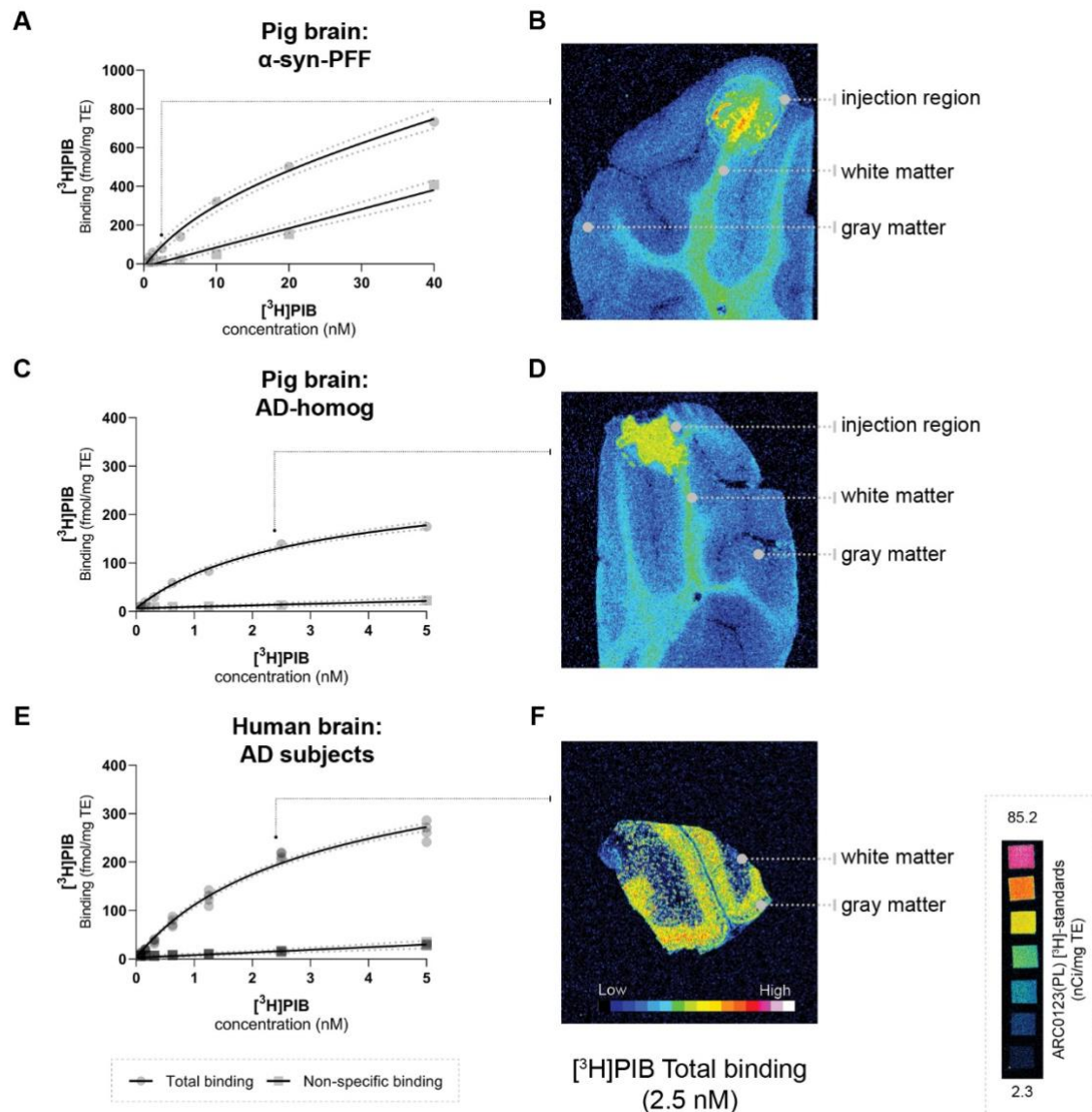
Regions	Kinetic Modelling Outcome	
	V_T (ml/cm ³)	BP_{ND}
α -syn-PFF	47.7 ± 6.3	0.65 ± 0.18
AD-homogenate	118.1 ± 12.9	2.34 ± 0.31
DLB-homogenate	31.1 ± 6.1	0.11 ± 0.16
Saline	21.2 ± 6.1	0.05 ± 0.03
Occipital cortex	23.8 ± 5.5	NA (reference)
Cerebellum	25.8 ± 6.8	0.01 ± 0.03

307

308 3.3 Characterization of the injection site

309 Using our minimally invasive method, we successfully injected all animals in the same symmetrical
 310 brain region. Prefrontal cortical immunostaining (α -synuclein and amyloid- β) and thioflavin S
 311 staining at the injection site confirmed the presence of α -synuclein preformed fibrils, AD
 312 homogenates, and DLB homogenates, respectively (Supplementary information). To evaluate the
 313 appropriateness of our pig model, we compared B_{max} and K_D in both the pig and human brains. This
 314 was done for the α -synuclein-preformed fibrils and AD-homogenate injected pig brain regions as
 315 well as for the AD postmortem human brain slices using $[^3\text{H}]PIB$ autoradiography saturation assays
 316 (Figure 4 and Table 3). We determined B_{max} to be 477.2 fmol/mg TE and K_D of 12.07 nM in the α -

317 synuclein-preformed fibrils region in pig brain slices (n=1). We found a higher B_{\max} on the AD
 318 postmortem human brain slices (366.7 fmol/mg TE, n=3) compared to AD-homogenate-injected pig
 319 brain slices (233.4 fmol/mg TE, n=1). However, the K_D is similar at 2.46 nM in AD-homogenate-
 320 injected pig brain slices versus 2.54 nM in AD postmortem human brain slices. We also found 2.4
 321 times higher binding potential in AD-homogenate-injected pig brain slices compared to α -synuclein-
 322 preformed fibrils-injected pig brain slices.



323

324 **Figure 4.** Saturation assays (A, C, E) and: corresponding representative autoradiograms (B, D, F
 325 [total binding at 2.5 nM]) of $[^3\text{H}]$ PIB in the pig brain: A: α -syn-PFF injected, D: AD-homogenate
 326 injected, and F) Human AD brain. Scale (ARC0123(PL)) inserted.

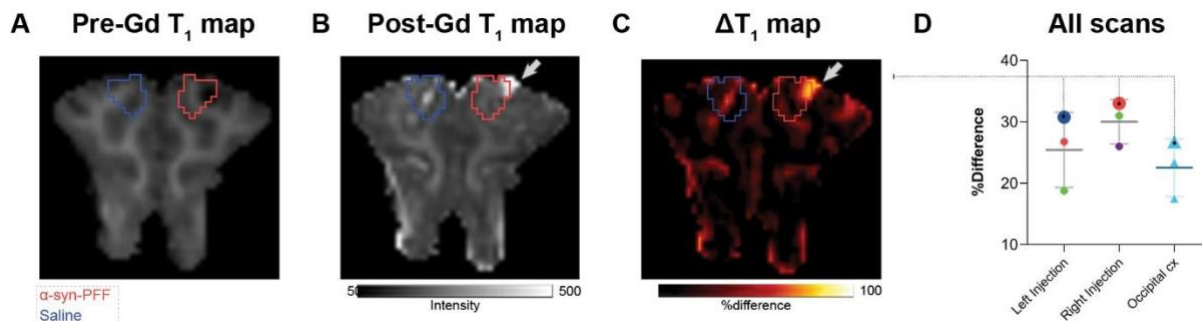
327 **Table 3.** Summary of B_{\max} and K_D . Values (95% confidence interval) from $[^3\text{H}]$ PIB saturation assays
 328 performed on injected pigs and humans frozen brain sections. n= number of unique individuals. BP=
 329 binding potential.

330

Sections	n	B_{max} (fmol/mg TE)	K_D (nM)	BP
Pig brain α -syn-PFF injected	1	477.2 (353.2 to 682.6)	12.07 (5.70 to 25.94)	39.53
Pig brain AD-homogenate injected	1	233.4 (202.3 to 273.8)	2.46 (1.83 to 3.35)	94.87
Human brain AD patients	2 (2 regions)	366.7 (332.8 to 407.0)	2.54 (2.09 to 3.12)	144.37

331 3.4 Blood-brain barrier integrity

332 We found no statistically significant difference in the T_1 -maps before and after gadolinium injection.
333 Still, in cases, with local hemorrhage near the site of needle penetration (Figure 5A, red ROI), some
334 regions had higher gadolinium uptake than the occipital cortex. Also, the amplitude of the [^{11}C]PIB
335 time-activity curves (Figure 2B and Figure 3) did not suggest that the injected regions had higher
336 uptake compared to non-injured brain tissue. Finally, the uptake in saline-injected regions did not
337 differ from that of the occipital cortex, supporting that the injection itself does not hamper the
338 integrity of the BBB.



339

340 **Figure 5.** Representative pre- (A) and post- (B) gadolinium-enhanced MRI of the injected region.
341 ΔT_1 maps are shown as %difference, i.e. % (post-Gd - pre-Gd) / pre-Gd. The right and left injection
342 regions (Right Injection vs. Left Injection) were compared to the occipital cortex. Data points were
343 color-coded for the different injections with larger symbols from the animals shown in A-C: red
344 circles = α -synuclein preformed fibrils injected region, dark blue circle = saline injected region, green
345 circles = DLB homogenate injected region, purple circle = AD homogenate injected region, and light
346 blue triangles = occipital cortex.

347 4 Discussion

348 We here describe a large animal model for testing radioligands against specific targets, such as
349 abnormally configured protein structures, and the study is built on amyloid- β and its radiotracer
350 [^{11}C]PIB (Lockhart et al., 2007; Hellström-Lindahl et al., 2014). Such a large animal model is
351 valuable in addition to rodent studies because of the pig's larger and gyrate brain. We show that
352 when the pig brain is injected with synthetic proteins or brain homogenates, the blood-brain barrier

353 remains intact, the injected region's protein levels are comparable to the characteristics in the human
354 brain, and the *in vivo* binding characteristics allow for realistic quantification.

355 We validated our acute model by injecting α -synuclein preformed fibrils, AD human brain
356 homogenate, or DLB human brain homogenate in pigs' mPFC and visualized these regions *in vivo*
357 using [^{11}C]PIB PET. [^{11}C]PIB uptake in the injection site was used as a proof of concept for this
358 model. We found high regional [^{11}C]PIB uptake in the AD homogenate and moderate uptake in α -
359 synuclein preformed fibril injected regions. We also confirmed absence of specific uptake or binding
360 of the radioligand in DLB homogenate injected or saline injected regions. Collectively, these results
361 suggest that the model provides a tool for preclinical characterization of novel radioligands, including
362 collecting information about the pharmacokinetics and affinities of the brain pathology.

363 [^{11}C]PIB is a well-characterized radioligand for amyloid- β plaques (Price et al., 2005; Peretti et al.,
364 2019), routinely used to quantify amyloid- β plaques and for differential diagnosis and staging in
365 neurodegenerative diseases. Although [^{11}C]PIB has the highest affinity to amyloid plaques, it also
366 displays affinity towards other β -sheet structures like tau and α -synuclein. We chose to use [^{11}C]PIB
367 as proof of concept since it shows affinity to α -synuclein preformed fibrils (Fodero-Tavoletti et al.,
368 2007; Ye et al., 2008) and AD brain homogenates (Klunk et al., 2004; Lockhart et al., 2007). By
369 contrast, and as a negative control, [^{11}C]PIB has no affinity to Lewy bodies commonly seen in PD or
370 DLB histology (Fodero-Tavoletti et al., 2007; Ye et al., 2008), which we also confirmed both *in vivo*
371 and *in vitro*.

372 To the best of our knowledge, this is the first time [^{11}C]PIB has been tested in pigs with full arterial
373 blood sampling and kinetic modeling. Our laboratory and Aarhus University (Alstrup et al., 2018)
374 have previously performed [^{11}C]PIB scans in pigs (unpublished), where the data was quantified using
375 reference tissue modeling. Invasive kinetic modeling with [^{11}C]PIB was challenging since the 1-
376 tissue compartment model yielded a poor fit, while the 2-tissue compartment model failed, most
377 likely because of the very fast metabolism of the parent compound. Instead, we used the graphical
378 method, i.e., Logan Graphical analysis. We also used the SRTM2 with the occipital cortex as a
379 reference region (Yaqub et al., 2008; Tolboom et al., 2009). In humans, SRTM2 modeling of
380 [^{11}C]PIB is commonly used with the cerebellum as the reference region, but when that was attempted
381 in the pig brain, we got negative BP_{ND} values in DLB injected, saline injected and occipital cortex.
382 Hence, we used the occipital cortex instead as a reference region.

383 Postmortem human brain homogenates from patients with relevant neurodegenerative disorders were
384 introduced to "humanize" the pig model. We evaluated that the B_{max} in the injected pig brain was
385 realistically representing what is seen in the individuals with AD who served as the donors of tissue
386 homogenate. The observation that we found slightly lower B_{max} values in pig brain slices representing
387 the AD homogenate injected regions compared to human brain slices from AD patients confirms the
388 suitability of our pig model. We also performed a [^3H]PIB saturation assay on the α -synuclein
389 preformed fibril injected pig brain slices. Compared to the AD homogenate slices, the α -synuclein
390 preformed fibril injected pig brain slices had a 2.4-times lower BP_{ND} , as we also found in the *in vivo*
391 PET studies. It can be argued that injection of human brain homogenates provides a more realistic
392 model of the human AD brain compared to synthetic protein injections with, e.g., preformed fibrils
393 but in any instance, the synthesized protein must be thoroughly evaluated *in vitro* before using it the
394 model. In the current study, we used the highest available concentration of all the injectates for proof
395 of concept. As an added value of the model in future studies, the concentration of the injectates can
396 be varied to confirm the expected dose-dependent effect of radioligand binding.

397 Whereas strategy of intracerebrally injecting α -synuclein (and amyloid- β) and scanning animals
398 immediately after previously has been used in rodents (Verdurand et al., 2018; Kuebler et al., 2020),
399 this is the first study to involve larger animals. A few other large animal models of α -synuclein
400 pathology have been published: the viral-vector model in minipigs (Lillethorup et al., 2018) and
401 nonhuman primates (Kirik et al., 2002; Yang et al., 2015; Koprich et al., 2016), and α -synuclein
402 protein or homogenate inoculation models also in nonhuman primates (Recasens et al., 2014;
403 Shimozawa et al., 2017). The disadvantages of these models are that they are challenging to create,
404 expensive to maintain and it often take months to develop pathology. National regulations on ethical
405 considerations can also restrict access to experimental studies in nonhuman primates. By contrast,
406 our model combines surgery and scanning on the same day, using non-survival pigs and a systematic
407 scanning technique for in vivo radioligand characterization (Ettrup et al., 2013; Andersen et al., 2015;
408 Jørgensen et al., 2018). Studies in pigs are cheaper than other large animals as the use of pigs is
409 considered less ethically challenging.

410 Conventional strategies for intracerebral injection involve an MR-guided stereotactic approach (Glud
411 et al., 2011). This requires MR-guided calculation of the stereotactic coordinates prior to surgery for
412 the injection, which is a tedious and time-consuming procedure. In the present study, we employed a
413 minimally invasive approach with a modified stereotactic instrument and a previously validated
414 target point in the grey matter of mPFC (Jørgensen et al., 2017, 2018), which made the procedure
415 much faster; the process including injection of the experimental substrates in mPFC was completed
416 within 3-4 hours. The concern whether the blood-brain barrier would retain its integrity right after the
417 intracerebral injection was addressed by the finding that the gadolinium-enhanced post-injection MR
418 assured no blood-brain barrier leakage, except in the cases where the needle had induced minor
419 traumatic hemorrhage – this was clearly outside the region with pathology. This observation was
420 further supported by the saline-injected region having a radioligand uptake similar to the reference
421 regions (Table 2).

422 Some limitations with the model presented should be mentioned. Although this model can be used
423 for survival studies, we have only validated bilateral injection sites in the medial prefrontal cortex. A
424 thorough in vitro evaluation of the proteins is necessary before commencing in vivo experiments,
425 preferably including autoradiography with the radioligand to be evaluated. The latter includes
426 identification of K_D and B_{max} to establish the in vitro binding potential which should reflect the PET
427 signal. Further, the injection site constitutes a relatively small volume of interest which inherently is
428 prone to noisy time-activity curves or to partial volume effect. Further, bleeding from dura or the
429 cerebral tissue resulting from the injection could potentially impact the PET signal. We saw confined
430 hematomas in 1 out of 5 injections but this was clearly recognized and when taken into account, it
431 did not prevent a proper analysis. For future use of the model, we recommend to use hybrid PET/CT
432 or PET/MR so that eventual hemorrhage can be accounted for.

433 5 Conclusions

434 We here provide a novel large model for assessment of novel radioligands targeting the brain and
435 show its suitability for testing radioligands for brain regional proteinopathies. The large pig brain
436 makes it suitable for neurosurgical procedures and the pigs can undergo multiple PET scans and
437 frequent blood sampling. The described pig model represents a robust and efficient set-up with few
438 limitations. The availability of a large animal α -synuclein model is instrumental for testing novel
439 radioligands, not only for α -synuclein neuroimaging but also for other target proteins where the target
440 is not naturally occurring in the brain, or where the presence can be artificially enhanced locally in
441 the brain.

442

443 **6 Acknowledgments**



444

445 This project has received funding from the European Union's Horizon 2020 research and innovation
446 program under the Marie Skłodowska-Curie grant agreement No. 813528. This project also received
447 funding from Parkinson foreningen, Denmark (R16-A247). Pontus Plavén Sigray was supported by
448 the Lundbeck Foundation (R303-2018-3263). Natalie Beschorner was supported by the Lundbeck
449 Foundation (R322-2019-2744). We would like to express our sincere gratitude to Patrick MacDonald
450 Fisher for his technical assistance in MRI scanning protocols and data processing. We want to thank
451 Lundbeck A/S, Valby, Denmark, for providing the α -synuclein preformed fibrils. This research
452 project received human brain tissue from the Neuropathology Core of the Emory Center for
453 Neurodegenerative Disease; we are grateful for their support. We would sincerely like to thank the
454 staff and veterinarians at EMED, Panum, København University.

455 **7 Author Contributions**

456 NRR, LMJ, GMK: conceptualization and design. NRR, LMJ: surgical setup. NRR, AN, CAM, NB,
457 EEB, SL: experimental studies. NRR, AN, CS, SL, PPS, MJ: analysis and software. NRR, GMK:
458 resources. NR, PPS, LMJ, GMK: data curation. NRR: preparation of manuscript draft including
459 figures. NRR, AN, CAM, NB, EEB, MJ, SL, MPP, CS, PPS, LMJ, GMK: manuscript review and
460 editing. MP, CS, PPS, LMJ, GMK: supervision. NRR, MP, GMK: funding acquisition. All authors
461 have read and agreed to the published version of the manuscript.

462 **8 Conflict of Interest**

463 Lundbeck A/S, Denmark provided the α -synuclein preformed fibrils as part of the European Union's
464 Horizon 2020 research and innovation program under the Marie Skłodowska-Curie grant agreement
465 No. 813528. However, they had no other financial interests in the project. GMK received honoraria
466 as a speaker and consultant for Sage Pharmaceuticals/Biogen and Sanos A/S. All other authors
467 declare no conflict of interest.

468 **9 Data availability statement**

469 All data, including MATLAB and R scripts, is available at a GitHub repository
470 (https://github.com/nakulrraval/Protien_inj_pig_model_PIB). All other requests are directed to this
471 article's corresponding or first author.

472 **10 References:**

473 Alstrup, A. K. O., Munk, O. L., and Landau, A. M. (2018). PET radioligand injection for pig
474 neuroimaging. *of Laboratory Animal* ... 44. Available at:
475 <http://sjlas.org/index.php/SJLAS/article/view/509>.

476 Braak, H., and Braak, E. (2000). Pathoanatomy of Parkinson's disease. *J. Neurol.* 247 Suppl 2, II3–
477 10. doi:10.1007/PL00007758.

478 Capotosti, F., Vokali, E., Molette, J., Tsika, E., Ravache, M., Juergens, T., et al. (2020). Developing a
479 novel alpha-synuclein positron emission tomography (PET) tracer for the diagnosis of
480 synucleinopathies. *Alzheimers. Dement.* 16. doi:10.1002/alz.043249.

481 Donovan, L. L., Magnussen, J. H., Dyssegard, A., Lehel, S., Hooker, J. M., Knudsen, G. M., et al.
482 (2020). Imaging HDACs In Vivo: Cross-Validation of the [11 C]Martinostat Radioligand in the
483 Pig Brain. *Mol. Imaging Biol.* 22, 569–577. doi:10.1007/s11307-019-01403-9.

484 Dunn, O. J. (1964). Multiple Comparisons Using Rank Sums. *Technometrics* 6, 241–252.
485 doi:10.1080/00401706.1964.10490181.

486 Ettrup, A., Holm, S., Hansen, M., Wasim, M., Santini, M. A., Palner, M., et al. (2013). Preclinical
487 safety assessment of the 5-HT2A receptor agonist PET radioligand [11C]cimbi-36. *Mol.*
488 *Imaging Biol.* 15, 376–383. doi:10.1007/s11307-012-0609-4.

489 Fodero-Tavoletti, M. T., Smith, D. P., McLean, C. A., Adlard, P. A., Barnham, K. J., Foster, L. E., et
490 al. (2007). In vitro characterization of Pittsburgh compound-B binding to Lewy bodies. *J.*
491 *Neurosci.* 27, 10365–10371. doi:10.1523/JNEUROSCI.0630-07.2007.

492 Gillings, N. (2009). A restricted access material for rapid analysis of [(11)C]-labeled
493 radiopharmaceuticals and their metabolites in plasma. *Nucl. Med. Biol.* 36, 961–965.
494 doi:10.1016/j.nucmedbio.2009.07.004.

495 Glud, A. N., Hedegaard, C., Nielsen, M. S., Sørensen, J. C., Bendixen, C., Jensen, P. H., et al.
496 (2011). Direct MRI-guided stereotaxic viral mediated gene transfer of alpha-synuclein in the
497 Göttingen minipig CNS. *Acta Neurobiol. Exp.* 71, 508–518. Available at:
498 <https://www.ncbi.nlm.nih.gov/pubmed/22237496>.

499 Hansen, H. D., Herth, M. M., Ettrup, A., Andersen, V. L., Lehel, S., Dyssegard, A., et al. (2014).
500 Radiosynthesis and in vivo evaluation of novel radioligands for pet imaging of cerebral 5-ht7
501 receptors. *J. Nucl. Med.* 55, 640–646. doi:10.2967/jnumed.113.128983.

502 Harding, J. D. (2017). Nonhuman Primates and Translational Research: Progress, Opportunities, and
503 Challenges. *ILAR J.* 58, 141–150. doi:10.1093/ilar/ilx033.

504 Hellström-Lindahl, E., Westermark, P., Antoni, G., and Estrada, S. (2014). In vitro binding of
505 [³H]PIB to human amyloid deposits of different types. *Amyloid* 21, 21–27.
506 doi:10.3109/13506129.2013.860895.

507 Hooshyar Yousefi, B., Shi, K., Arzberger, T., Wester, H. J., Schwaiger, M., Yakushev, I., et al.
508 (2019). Translational study of a novel alpha-synuclein PET tracer designed for first-in-human
509 investigating. in *NuklearMedizin 2019* (Georg Thieme Verlag KG), L25. doi:10.1055/s-0039-
510 1683494.

511 Jørgensen, L. M., Baandrup, A. O., Mandeville, J., Glud, A. N., Sørensen, J. C. H., Weikop, P., et al.
512 (2021). An fMRI-compatible system for targeted electrical stimulation. *Research Square*.
513 doi:10.21203/rs.3.rs-313183/v1.

514 Jørgensen, L. M., Weikop, P., Svarer, C., Feng, L., Keller, S. H., and Knudsen, G. M. (2018).
515 Cerebral serotonin release correlates with [11C]AZ10419369 PET measures of 5-HT1B receptor
516 binding in the pig brain. *J. Cereb. Blood Flow Metab.* 38, 1243–1252.

517 doi:10.1177/0271678X17719390.

518 Jørgensen, L. M., Weikop, P., Villadsen, J., Visnapuu, T., Ettrup, A., Hansen, H. D., et al. (2017).
519 Cerebral 5-HT release correlates with [11C]Cimbi36 PET measures of 5-HT2A receptor
520 occupancy in the pig brain. *J. Cereb. Blood Flow Metab.* 37, 425–434.
521 doi:10.1177/0271678X16629483.

522 Kaide, S., Watanabe, H., Shimizu, Y., Iikuni, S., Nakamoto, Y., Hasegawa, M., et al. (2020).
523 Identification and Evaluation of Bisquinoline Scaffold as a New Candidate for α -Synuclein-PET
524 imaging. *ACS Chem. Neurosci.* 11, 4254–4261. doi:10.1021/acschemneuro.0c00523.

525 Keller, S. H., Svarer, C., and Sibomana, M. (2013). Attenuation correction for the HRRT PET-
526 scanner using transmission scatter correction and total variation regularization. *IEEE Trans.*
527 *Med. Imaging* 32, 1611–1621. doi:10.1109/TMI.2013.2261313.

528 Kirik, D., Rosenblad, C., Burger, C., Lundberg, C., Johansen, T. E., Muzyczka, N., et al. (2002).
529 Parkinson-Like Neurodegeneration Induced by Targeted Overexpression of α -Synuclein in the
530 Nigrostriatal System. *Journal of Neuroscience* 22, 2780–2791. doi:10.1523/JNEUROSCI.22-07-
531 02780.2002.

532 Klunk, W. E., Engler, H., Nordberg, A., Wang, Y., Blomqvist, G., Holt, D. P., et al. (2004). Imaging
533 brain amyloid in Alzheimer's disease with Pittsburgh Compound-B. *Ann. Neurol.* 55, 306–319.
534 doi:10.1002/ana.20009.

535 Koprlich, J. B., Johnston, T. H., Reyes, G., and Omana, V. (2016). Towards a nonhuman primate
536 model of alpha-synucleinopathy for development of therapeutics for Parkinson's disease:
537 optimization of AAV1/2 delivery *PLoS*. Available at:
538 <https://journals.plos.org/plosone/article?id=10.1371/journal.pone.0167235>.

539 Korat, Š., Bidesi, N. S. R., Bonanno, F., Di Nanni, A., Hoàng, A. N. N., Herfert, K., et al. (2021).
540 Alpha-Synuclein PET Tracer Development—An Overview about Current Efforts.
541 *Pharmaceuticals* 14, 847. doi:10.3390/ph14090847.

542 Kuebler, L., Buss, S., Leonov, A., Ryazanov, S., Schmidt, F., Maurer, A., et al. (2020).
543 [11C]MODAG-001—towards a PET tracer targeting α -synuclein aggregates. *Eur. J. Nucl. Med.*
544 *Mol. Imaging*. doi:10.1007/s00259-020-05133-x.

545 Lashuel, H. A., Overk, C. R., Oueslati, A., and Masliah, E. (2013). The many faces of α -synuclein:
546 from structure and toxicity to therapeutic target. *Nat. Rev. Neurosci.* 14, 38–48.
547 doi:10.1038/nrn3406.

548 Lázaro, D. F., Bellucci, A., Brundin, P., and Outeiro, T. F. (2019). Editorial: Protein Misfolding and
549 Spreading Pathology in Neurodegenerative Diseases. *Front. Mol. Neurosci.* 12, 312.
550 doi:10.3389/fnmol.2019.00312.

551 Lillethorup, T. P., Glud, A. N., Landeck, N., Alstrup, A. K. O., Jakobsen, S., Vang, K., et al. (2018).
552 In vivo quantification of glial activation in minipigs overexpressing human α -synuclein. *Synapse*
553 72, e22060. doi:10.1002/syn.22060.

554 Li, X., Morgan, P. S., Ashburner, J., Smith, J., and Rorden, C. (2016). The first step for
555 neuroimaging data analysis: DICOM to NIfTI conversion. *J. Neurosci. Methods* 264, 47–56.

556 doi:10.1016/j.jneumeth.2016.03.001.

557 Lockhart, A., Lamb, J. R., Osredkar, T., Sue, L. I., Joyce, J. N., Ye, L., et al. (2007). PIB is a non-
558 specific imaging marker of amyloid-beta (Abeta) peptide-related cerebral amyloidosis. *Brain*
559 130, 2607–2615. doi:10.1093/brain/awm191.

560 Logan, J., Fowler, J. S., Volkow, N. D., Wolf, A. P., Dewey, S. L., Schlyer, D. J., et al. (1990).
561 Graphical analysis of reversible radioligand binding from time-activity measurements applied to
562 [N-11C-methyl]-(-)-cocaine PET studies in human subjects. *J. Cereb. Blood Flow Metab.* 10,
563 740–747. doi:10.1038/jcbfm.1990.127.

564 Makky, A., Bousset, L., Polesel-Maris, J., and Melki, R. (2016). Nanomechanical properties of
565 distinct fibrillar polymorphs of the protein α -synuclein. *Sci. Rep.* 6, 37970.
566 doi:10.1038/srep37970.

567 Matheson, G. J. (2019). kinfitr: Reproducible PET Pharmacokinetic Modelling in R. *bioRxiv*,
568 755751. doi:10.1101/755751.

569 Mathis, C. A., Lopresti, B. J., Ikonomovic, M. D., and Klunk, W. E. (2017). Small-molecule PET
570 Tracers for Imaging Proteinopathies. *Semin. Nucl. Med.* 47, 553–575.
571 doi:10.1053/j.semnuclmed.2017.06.003.

572 Parker, C. A., Gunn, R. N., Rabiner, E. A., Slifstein, M., Comley, R., Salinas, C., et al. (2012).
573 Radiosynthesis and characterization of 11C-GSK215083 as a PET radioligand for the 5-HT6
574 receptor. *J. Nucl. Med.* 53, 295–303. doi:10.2967/jnumed.111.093419.

575 Peretti, D. E., Reesink, F. E., Doorduin, J., de Jong, B. M., De Deyn, P. P., Dierckx, R. A. J. O., et al.
576 (2019). Optimization of the k2' Parameter Estimation for the Pharmacokinetic Modeling of
577 Dynamic PIB PET Scans Using SRTM2. *Frontiers in Physics* 7, 212.
578 doi:10.3389/fphy.2019.00212.

579 Price, J. C., Klunk, W. E., Lopresti, B. J., Lu, X., Hoge, J. A., Ziolko, S. K., et al. (2005). Kinetic
580 modeling of amyloid binding in humans using PET imaging and Pittsburgh Compound-B. *J.*
581 *Cereb. Blood Flow Metab.* 25, 1528–1547. doi:10.1038/sj.jcbfm.9600146.

582 Recasens, A., Dehay, B., Bové, J., Carballo-Carbalal, I., Dovero, S., Pérez-Villalba, A., et al. (2014).
583 Lewy body extracts from Parkinson disease brains trigger α -synuclein pathology and
584 neurodegeneration in mice and monkeys. *Ann. Neurol.* 75, 351–362. doi:10.1002/ana.24066.

585 Saikali, S., Meurice, P., Sauleau, P., Eliat, P.-A., Bellaud, P., Randuineau, G., et al. (2010). A three-
586 dimensional digital segmented and deformable brain atlas of the domestic pig. *J. Neurosci.*
587 *Methods* 192, 102–109. doi:10.1016/j.jneumeth.2010.07.041.

588 Schneider, C. A., Rasband, W. S., and Eliceiri, K. W. (2012). NIH Image to ImageJ: 25 years of
589 Image Analysis HHS Public Access.

590 Shalgunov, V., Xiong, M., L'Estrade, E. T., Raval, N. R., Andersen, I. V., Edgar, F. G., et al. (2020).
591 Blocking of efflux transporters in rats improves translational validation of brain radioligands.
592 *EJNMMI Res.* 10, 124. doi:10.1186/s13550-020-00718-x.

593 Shimozawa, A., Ono, M., Takahara, D., Tarutani, A., Imura, S., Masuda-Suzukake, M., et al. (2017).

594 Propagation of pathological α -synuclein in marmoset brain. *Acta Neuropathol Commun* 5, 12.
595 doi:10.1186/s40478-017-0413-0.

596 Sureau, F. C., Reader, A. J., Comtat, C., Leroy, C., Ribeiro, M. J., Buvat, I., et al. (2008). Impact of
597 image-space resolution modeling for studies with the high-resolution research tomograph. *J.
598 Nucl. Med.* 49, 1000–1008. doi:10.2967/jnumed.107.045351.

599 Tjerkaski, J., Cervenka, S., Farde, L., and Matheson, G. J. (2020). Kinfitr - an open-source tool for
600 reproducible PET modelling: validation and evaluation of test-retest reliability. *EJNMMI Res.*
601 10, 77. doi:10.1186/s13550-020-00664-8.

602 Tolboom, N., Yaqub, M., Boellaard, R., Luurtsema, G., Windhorst, A. D., Scheltens, P., et al. (2009).
603 Test-retest variability of quantitative [^{11}C]PIB studies in Alzheimer's disease. *Eur. J. Nucl. Med.
604 Mol. Imaging* 36, 1629–1638. doi:10.1007/s00259-009-1129-6.

605 Verdurand, M., Levigoureux, E., Zeinyeh, W., Berthier, L., Mendjel-Herda, M., Cadarossanesaib, F.,
606 et al. (2018). In Silico, in Vitro, and in Vivo Evaluation of New Candidates for α -Synuclein PET
607 Imaging. *Mol. Pharm.* 15, 3153–3166. doi:10.1021/acs.molpharmaceut.8b00229.

608 Villadsen, J., Hansen, H. D., Jørgensen, L. M., Keller, S. H., Andersen, F. L., Petersen, I. N., et al.
609 (2017). Automatic delineation of brain regions on MRI and PET images from the pig. *J.
610 Neurosci. Methods* 294, 51–58. doi:10.1016/j.jneumeth.2017.11.008.

611 Winterdahl, M., Audrain, H., Landau, A. M., Smith, D. F., Bonaventure, P., Shoblock, J. R., et al.
612 (2014). PET brain imaging of neuropeptide Y2 receptors using N- ^{11}C -methyl-JNJ-31020028 in
613 pigs. *J. Nucl. Med.* 55, 635–639. doi:10.2967/jnumed.113.125351.

614 Yang, W., Wang, G., Wang, C.-E., Guo, X., Yin, P., Gao, J., et al. (2015). Mutant Alpha-Synuclein
615 Causes Age-Dependent Neuropathology in Monkey Brain. *Journal of Neuroscience* 35, 8345–
616 8358. doi:10.1523/JNEUROSCI.0772-15.2015.

617 Yaqub, M., Tolboom, N., Boellaard, R., van Berckel, B. N. M., van Tilburg, E. W., Luurtsema, G., et
618 al. (2008). Simplified parametric methods for [^{11}C]PIB studies. *Neuroimage* 42, 76–86.
619 doi:10.1016/j.neuroimage.2008.04.251.

620 Ye, L., Velasco, A., Fraser, G., Beach, T. G., Sue, L., Osredkar, T., et al. (2008). In vitro high affinity
621 alpha-synuclein binding sites for the amyloid imaging agent PIB are not matched by binding to
622 Lewy bodies in postmortem human brain. *J. Neurochem.* 105, 1428–1437. doi:10.1111/j.1471-
623 4159.2008.05245.x.

624 Lammertsma, A. A., and Hume, S. P. (1996). Simplified reference tissue model for PET receptor
625 studies. *Neuroimage* 4, 153–158. doi:10.1006/nimg.1996.0066.